THE ASTROPHYSICAL JOURNAL, 513:679–689, 1999 March 10


# IMAGES AND SPECTRA FROM THE INTERIOR OF A RELATIVISTIC FIREBALL

JONATHAN GRANOT, TSVI PIRAN, AND RE'EM SARI
Racah Institute, Hebrew University, Jerusalem 91904, Israel; jgranot@nikki.fiz.huji.ac.il, tsvi@nikki.fiz.huji.ac.il, sari@nikki.fiz.huji.ac.il
*Received 1998 June 15; accepted 1998 October 19*

## ABSTRACT

The power-law decay of gamma-ray burst (GRB) afterglow can be well described by synchrotron emission from a relativistic spherical blast wave, driven by an expanding fireball. We calculate the spectrum and the light curve expected from an adiabatic blast wave which is described by the Blandford-McKee self-similar solution. These calculations include emission from the whole blast wave and not just from the shock front. We provide numerical corrections that can be used to modify simple analytic estimates of such emission. We find that the expected light curve and spectra are flat near the peak. This rules out the interpretation of the sharp optical peak observed in GRB 970508 as the peak of the light curve. We also calculate the observed image of an afterglow. This image could be resolved in future VLBI observations, and its structure could influence microlensing and scintillation. The observed image is ringlike: brighter near the edge and dimmer at the center. The image depends on the observed frequency. The contrast between the edge and the center increases and the ring becomes narrower at higher frequencies.

*Subject headings:* gamma rays: bursts — gamma rays: theory — hydrodynamics — magnetic fields — relativity — shock waves

## 1. INTRODUCTION

The delayed X-ray, optical, and radio emission "afterglow" following a gamma-ray burst (GRB) was predicted as a natural outcome of the fireball model (Paczyński & Rhoads 1993; Katz 1994; Mészáros & Rees 1997; Sari & Piran 1997). It is reasonably described by emission from a spherical relativistic shell, decelerating upon collision with an ambient medium (Waxman 1997a; Mészáros & Rees 1997; Katz & Piran 1997; Sari, Piran, & Narayan 1998). A relativistic blast wave is formed and expands through the surrounding medium, heating the matter in its wake. The observed afterglow is believed to be due to synchrotron emission of relativistic electrons from the heated matter. The surrounding medium will be referred to as interstellar medium (ISM), although this may not necessarily be the case.

At any given time, a detector receives photons that were emitted at different times in the observer frame, at different distances behind the shock front, and at different angles from the line of sight (LOS) to the center of the shell. The properties of the matter are different at each of these points, and so are the emissivity and the frequency of the emitted radiation. Early calculations have considered emission from a single representative point (Mészáros & Rees 1997; Waxman 1997a; Sari et al. 1998). Later works have included more detailed calculations. Synchrotron emission was considered from the shock front (Sari 1998; Panaitescu & Mészáros 1998), and monochromatic emission was considered from a uniform shell (Waxman 1997c).

Even if the electrons carry a large fraction of the internal energy, the hydrodynamic evolution becomes adiabatic after a short time, when the electrons can no longer cool efficiently (Sari et al. 1998). For reasonable values of the burst parameters this transition takes place approximately an hour after the GRB. The adiabatic solution is valid from there onward. Numerical simulations of the evolution of a generic relativistic adiabatic fireball with arbitrary initial conditions have shown that the solution converges quickly to the Blandford-McKee (1976, hereafter BM) self-similar solution. In the following we consider, therefore, synchrotron emission from this solution.

We neglect scattering, self-absorption, and electron cooling. Self-absorption becomes important at frequencies much smaller than the peak frequency, and for slow cooling, electron cooling becomes important at frequencies much higher than the peak frequency, so this should yield a good approximation for the observed flux density around the peak. An analysis of the spectrum over a wider range of frequencies was made by Sari et al. (1998).

In § 2 we derive the basic formula for the observed flux density from a system moving relativistically. We present the underlying physical model: synchrotron emission from a power-law electron distribution in § 3. In § 4 we calculate the spectrum and the light curve. We show that both the light curve and the spectra are flat near the peak. This causes difficulty in explaining the shape of the optical peak of GRB 970508 (Sokolov et al. 1997). We compare our calculations of the peak frequency and the peak flux with those of a simpler analytic model. We provide a table for numerical corrections that can be used to modify the results of this model. We also compare the spectra and light curves with those of a uniform shell (Waxman 1997c). We show that the two results are quite different. This demonstrates the need to consider synchrotron emission from the full BM solution. In § 5 we consider three alternative magnetic field models. We show that the light curve and the spectrum do not vary significantly when we model the magnetic field differently. We calculate the surface brightness and obtain the observed image of a GRB afterglow in § 6. As indicated in previous works (Waxman 1997c; Sari 1998; Panaitescu & Mészáros 1998), the image is ringlike: it is brighter near the edge and dimmer near the center. At a given observed time, the contrast between the edge and the center of the image increases and the width of the ring decreases at higher frequencies.

We conclude, in § 7, with a summary of our results and a discussion of their observational implications.

## 2. THE FORMALISM

We consider a system that is moving relativistically while emitting radiation. We calculate the flux density that is measured by a distant detector (i.e., $D \gg L$, where $D$ is the distance to the detector and $L$ is the size of the area emitting radiation). We use a spherical coordinate system centered on the shell. The $z$-axis points toward the detector (see Fig. 1). The detector is at rest in this frame, and so is the ambient ISM. We refer to this frame as the observer frame. Consider a small volume element $dV = r^2\, dr\, d\mu\, d\phi$ (where $\mu \equiv \cos\theta$), and let $j'_{\nu'}$ be the energy per unit time per unit volume per unit frequency per unit solid angle, emitted by the matter within this volume in its local frame (note that generally $j_\nu$ depends on the direction $\Omega$ as well as on the frequency, place, and time). We denote quantities measured in the local rest frame of the matter with a prime, while quantities without a prime are measured in the observer frame. Note that $j_\nu/\nu^2$ is Lorentz invariant (Rybicki & Lightman 1979, chap. 4, p. 147) and $\nu' = \nu\gamma(1 - \beta\mu_\nu)$, where $\gamma$ and $\beta c$ are the Lorentz factor and the velocity of the matter emitting the radiation, respectively, and $\mu_\nu$ is the cosine of the angle between the direction of the velocity of the matter and the direction to the detector, in the observer frame. The contribution to $I_\nu$ from this volume element is given by

$$dI_\nu \cong j_\nu \frac{dr}{\mu} = \frac{j'_{\nu'}}{\gamma^2(1 - \beta\mu_\nu)^2}\frac{dr}{\mu} \tag{1}$$

(see Fig. 1). The contribution to the flux density at the detector is $dF_\nu \cong I_\nu\, d\Omega$, where $\Omega$ is the solid angle seen from the detector, and $I_\nu$ includes all the contributions from different volume elements along the trajectory arriving at the detector from the direction $\Omega$ simultaneously and at the time for which $F_\nu$ is calculated. Consider a photon emitted at time $t$ and place $\boldsymbol{r}$ in the observer frame. It will reach the detector at a time $T$ given by

$$T_z = \frac{T}{1+z} = t - \frac{r\mu}{c}\,, \tag{2}$$

where $z$ is the cosmological redshift of the GRB, and $T = 0$ was chosen as the time of arrival at the detector of a photon emitted at the origin at $t = 0$. Using $\alpha \cong r(1 - \mu^2)^{1/2}/D$, we obtain

$$F(\nu, T) = \frac{1+z}{d_L^2}\int_0^{2\pi} d\phi \int_{-1}^{1} d\mu \int_0^{\infty} r^2\, dr \times \frac{j'(\Omega'_d, \nu\gamma(1 - \beta\mu_\nu), \boldsymbol{r}, T_z + r\mu/c)}{\gamma^2(1 - \beta\mu_\nu)^2}\,, \tag{3}$$

where $d_L$ is the luminosity distance to the GRB, and $j' = j'(\Omega', \nu', \boldsymbol{r}, t)$, and later $P' = P'(\nu', \boldsymbol{r}, t)$; $j'$ is taken in the direction $\Omega'_d$ at which a photon should be emitted in order to reach the detector, and $\gamma$, $\beta$, $\mu_\nu$ should be taken at the time $t$ implied by equation (2).

For a spherical expanding system, which emits isotropically in its local rest frame, one obtains $\mu_\nu = \mu$ and $j'_\nu = P'_\nu/4\pi$, so that

$$F(\nu, T) = \frac{1+z}{2d_L^2}\int_{-1}^{1} d\mu \int_0^{\infty} r^2\, dr\, \frac{P'(\nu\gamma(1 - \beta\mu), r, T_z + r\mu/c)}{\gamma^2(1 - \beta\mu)^2}\,. \tag{4}$$

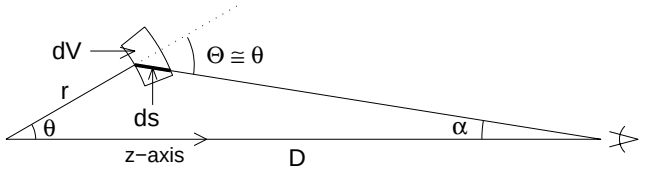


FIG. 1.—The contribution of a volume element $dV$ to the flux observed by a distant observer is $dF_\nu \approx dI_\nu\, d\Omega$, where $dI_\nu = j_\nu\, ds$. Since the observer is far away, the direction of emission in the observer frame is almost parallel to the $z$-axis.

Note that because of relativistic effects, a jet with an opening angle $\theta > 1/\gamma$ around the LOS can be considered locally as spherical (Piran 1994).

In order to learn whether the radial integration is important, we calculate the observed flux density from emission only along the LOS. We do this by considering a situation in which at each point the photons are emitted only radially: $j'_{\nu'} = P'_{\nu'}\,\delta(\Omega' - \Omega'(\hat{\boldsymbol{r}}))$. Note that the correct limit is obtained when the delta function in the direction of the emission is taken in the local frame. Since $d\Omega = \gamma^2(1 - \beta\mu)^2 d\Omega'$ (Rybicki & Lightman 1979, chap. 4, p. 141), we obtain

$$\delta(\Omega' - \Omega'(\hat{\boldsymbol{r}})) = \gamma^2(1 - \beta\mu)^2\delta(\Omega - \Omega(\hat{\boldsymbol{r}}))\,. \tag{5}$$

Substituting this $j'$ in equation (3), we obtain

$$F(\nu, T) = \frac{1+z}{d_L^2}\int_0^{\infty} r^2\, dr\, P'\left(\frac{\nu}{\gamma(1+\beta)}, r, T_z + \frac{r}{c}\right). \tag{6}$$

Equation (4) is quite general, and includes integration over all space. In the case of GRB afterglow, radiation is emitted only from the region behind the shock front. The spatial integration should therefore be taken over a finite volume, confined by the surface of the shock front. We would therefore like to obtain an explicit expression for the radius $R$ of the shock as a function of $\mu \equiv \cos\theta$ for a given arrival time $T$. In the case of a shell moving with a constant velocity $\beta c$, one obtains from equation (2)

$$R = \frac{\beta c T_z}{1 - \beta\mu}\,. \tag{7}$$

If one considers a constant arrival time $T$, this equation describes an ellipsoid, which confines the volume constituting the locus of points from which photons reach the detector simultaneously (Rees 1966). In GRBs, most of the matter is concentrated in a thin shell which decelerates upon collision with the ambient medium. When the deceleration of the shell is accounted for, the ellipsoid is distorted. The details of this distortion depend on the evolution of the shock radius $R(t)$ (Sari 1998; Panaitescu & Mészáros 1998). In this paper we consider an adiabatic ultrarelativistic hydrodynamic solution, which implies $\Gamma \propto R^{-3/2}$, where $\Gamma$ is the Lorentz factor of the shock. For this case, equation (2) yields

$$R = \frac{cT_z}{1 - \mu + 1/(8\Gamma^2)}\,. \tag{8}$$

The shape of the volume constituting the locus of points from which photons reach the detector simultaneously resembles an elongated egg (see Fig. 2) and will be simply referred to as "the egg." The side facing the observer (the

right side in the figures) will be referred to as the front of the egg, and the side closer to the origin (the left side in the figures) will be referred to as the back of the egg.

From hydrodynamic considerations, we expect the typical size of the region emitting radiation behind the shock to scale as $\Delta \propto R/\Gamma^2$ in the observer frame. Despite this fact, it is still important to consider the emission from the whole volume of the egg, whose limits are given by equation (8). To illustrate this, we give a simple example. Consider a photon emitted on the LOS at a distance $d = R/\gamma^2$ behind the shock (point A in Fig. 2) at a time $t_0$ in the observer frame, where $\gamma = \Gamma/\sqrt{2}$ is the Lorentz factor of the matter just behind the shock. This photon will catch up with the shock front at a later time $t_1$ in the observer frame (at point B in Fig. 2) and will arrive at the detector together with a photon emitted at that point at $t_1$. From equation (8) we find that, on the LOS, $R = 16\gamma^2 cT_z$, and so we obtain $R(t_1)/R(t_0) = 17^{1/4} \cong 2$. This shows that the emission comes from a substantial part of the volume of the egg, and not just from a thin layer near its surface. This is illustrated by the shaded region in Figures 7 and 9, which corresponds to a shell of width $\Delta = R/4\gamma^2$ in the observer frame.

At a given observed time $T$, the emission should be considered from the volume of the egg, whose surface is described by equation (8). Taking this into account, it is simpler to calculate the flux density at a given observed time $T$, using new variables $y$, $\chi$ that depend on $T$ (see Figs. 2 and 3):

$$y \equiv \frac{R}{R_l}, \quad \chi \equiv 1 + 16\gamma_f^2\left(\frac{R - r}{R}\right), \tag{9}$$

where $R = R(t)$ is the radius of the shock front, $\gamma_f$ is the Lorentz factor of the matter just behind the shock at the front of the radial profile, and $R_l$ is the radius of the point on the shock front, on the LOS, from which a photon

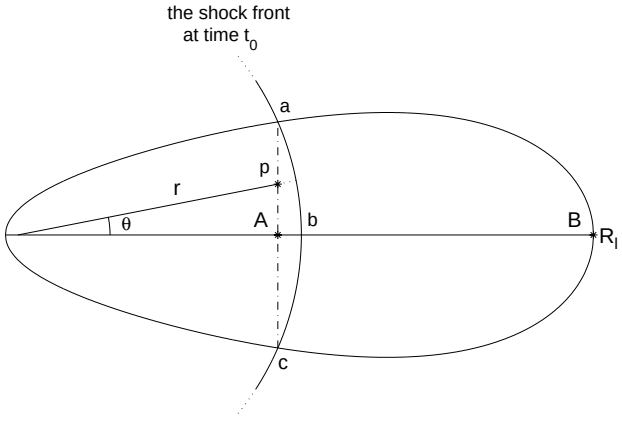


FIG. 2.—We see here the egg-shaped region from which photons reach an observer at a given time $T$. In all the figures of the "egg" the observer is located far to the right, and the symmetry axis is the LOS to the center of the GRB. In order to reach the observer simultaneously, photons emitted at different locations should be emitted at different times in the observer frame, according to eq. (2). Photons that are emitted simultaneously in the observer frame along the dash-dotted line *ac* reach the observer simultaneously. Therefore, *ac* represents an equal-$y$ contour line. The location of the shock front at this time of emission is indicated by the solid line *abc*, and its radius $R$ appears in the definitions of $y$, and $\chi$. A photon emitted at point A, at a distance of $d = r/\gamma^2$ behind the shock front and at a time $t_0$ (both in the observer frame) caches up with the shock front at point B, at a later time $t_1$ in the observer frame.

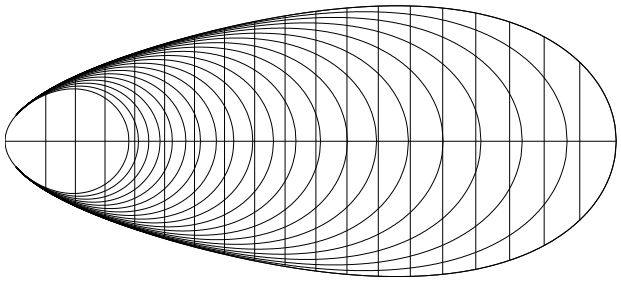

FIG. 3.—Equal-$y$ contour lines, $y = 0.1, 0.15, \ldots, 0.95$ (*vertical lines*); equal-$\chi$ contour lines, $\log_{10}\chi = 0, 0.15, 0.3, \ldots, 3$ (*curved lines*). The horizontal line is the LOS to the observer, which is located far to the right.

reaches the detector at a time $T$ (see Fig. 2). Since we expect the typical size of the emitting region behind the shock to scale as $\Delta \propto R/\gamma^2$, the choice of $\chi$ is natural to this problem. The exact form of $\chi$ was chosen to suit the BM solution, discussed below. Using equation (2) we can express $r$, $\mu$ in terms of $y$, $\chi$:

$$r \cong R_l\, y\,, \quad \mu \cong 1 - \frac{1 - \chi y^4}{16\gamma_l^2\, y}\,, \tag{10}$$

where $\gamma_l$ is the Lorentz factor of the matter just behind the shock, on the LOS.

We would like to express equation (4) in terms of $y$, $\chi$. This will enable us to calculate the flux density for the BM solution. This solution describes an adiabatic highly relativistic blast wave expanding into an ambient uniform and cold medium (Blandford & McKee 1976). In terms of $y$ and $\chi$ the BM solution is given by

$$n' = 4\gamma_f n_0\, \chi^{-5/4}, \quad \gamma = \gamma_f\, \chi^{-1/2}, \quad e' = 4n_0\, m_p c^2 \gamma_f^2\, \chi^{-17/12}\,, \tag{11}$$

where $n'$ and $e'$ are the number density and the energy density in the local frame, respectively, $\gamma$ is the Lorentz factor of the bulk motion of the matter behind the shock, $m_p$ is the mass of a proton, $n_0 = n_1 \times 1\ \mathrm{cm}^{-3}$ is the number density of the unshocked ambient ISM in its local rest frame, and $\gamma_f = \gamma_l\, y^{-3/2}$. For the BM solution, one obtains (Sari 1997)

$$\gamma_l \cong 3.65\left(\frac{E_{52}}{n_1}\right)^{1/8}\left(\frac{T_{\mathrm{days}}}{1+z}\right)^{-3/8},$$

$$R_l \cong 5.53 \times 10^{17}\left[\frac{E_{52}\, T_{\mathrm{days}}}{n_1(1+z)}\right]^{1/4} \mathrm{cm}\,, \tag{12}$$

where $E_{52}$ is the total energy of the shell in units of $10^{52}$ ergs, and $T_{\mathrm{days}}$ is the observed time in days.

For any spherically symmetric self similar solution we can define $g(\chi)$ by: $\gamma^2 \equiv \gamma_f^2\, g(\chi)$, where $g(\chi)$ describes how $\gamma$ varies with the radial profile. For the BM solution $g(\chi) = \chi^{-1}$, and for a uniform shell $g(\chi) = 1$. Using the definitions above, we obtain from equation (4) after the change of variables

$$F(\nu, T) = \frac{8R_l^3(1+z)}{d_L^2}\int_1^\infty d\chi \int_0^{\chi^{-1/4}} dy \times \frac{y^{10} P'(T_z, \nu\gamma(1-\beta\mu), y, \chi)}{\{1 + y^4[8g(\chi)^{-1} - \chi]\}^2 g(\chi)}\,. \tag{13}$$

This formula for the flux density takes into consideration the contribution from the whole volume behind the shock front, and will be referred to as the general formula.

We would like to single out the angular integration and the radial integration, in order to find out the different effects each integration has on the observed flux density. In order to single out the effect of the angular integration, we consider a thin shell of thickness $\Delta$ in the observer frame and take the limit $\Delta \to 0$. Because of kinematical spreading we expect $\Delta$ to scale as $\Delta \propto R/\gamma^2$. According to the definition of $\chi$, such a shell corresponds to a constant interval in $\chi$, i.e., the shell lies within the interval $\chi \in [1, \chi_{\max}]$ for some $\chi_{\max}$. The limit $\Delta \to 0$ corresponds to taking a delta function in $\chi$: $\delta(\chi - 1)$.

In order to single out the effect of the radial integration, we changed variables in equation (6) from $r$ to $\chi$. For the BM solution we obtain

$$F(\nu, T) = \frac{R_i^3(1+z)}{4d_L^2} \int_1^\infty d\chi\, \chi^{-7/4} P'\left(T_z, \frac{\nu}{\gamma(1+\beta)}, \chi\right). \quad (14)$$

## 3. THE PHYSICAL MODEL

According to the fireball model, a highly relativistic shell moves outward and is decelerated upon collision with the ambient ISM. This creates a relativistic blast wave that expands through the ISM and heats up the matter that passes through it. The relativistic electrons of the heated material emit synchrotron radiation in the presence of a magnetic field.

We now consider the synchrotron emission at a certain point, in which the values of $n'$, $\gamma$, and $e'$ are given by the hydrodynamic solution. In order to estimate the local emissivity, we assume that the energy of the electrons and of the magnetic field at each point are a fixed fraction of the total internal energy at that point: $e'_e = \epsilon_e e'$, $e'_B = \epsilon_B e'$. We assume that the shock produces a power-law electron distribution: $N(\gamma_e) = K\gamma_e^{-p}$ for $\gamma_e \geq \gamma_{\min}$ (for the energy of the electrons to remain finite we must have $p > 2$). In the figures for which a definite numerical value of $p$ is needed, we use $p = 2.5$. The constants $K$ and $\gamma_{\min}$ in the electron distribution can be calculated from the number density and energy density:

$$\gamma_{\min} = \left(\frac{p-2}{p-1}\right)\frac{\epsilon_e e'}{n' m_e c^2}, \quad K = (p-1)n'\gamma_{\min}^{p-1}, \quad (15)$$

where $m_e$ is the mass of the electron.

Assuming an isotropic velocity distribution, the total emitted power of a single average electron (i.e., with $\gamma_e = \langle\gamma_e\rangle$) is given by

$$P'_{e,\mathrm{av}} = \frac{4}{3}\sigma_{\mathrm{T}} c\beta^2 \langle\gamma_e\rangle^2 e'_B, \quad \langle\gamma_e\rangle \equiv \frac{\epsilon_e e'}{n' m_e c^2} \quad (16)$$

(Rybicki & Lightman 1979, chap. 6, p. 169), where $\sigma_{\mathrm{T}}$ is the Thomson cross section, and $e'_B = B^2/8\pi$, where $B$ is the magnetic field (in the local frame). Although we refer to the magnetic field in the local frame, throughout the paper, we make an exception and write it without a prime.

The synchrotron emission function (power per unit frequency) of a single electron is characterized by $P_{\nu,e} \propto \nu^{1/3}$ for frequencies much smaller than the electron synchrotron frequency, and it drops exponentially at large frequencies. The typical synchrotron frequency, averaged over an isotropic distribution of electron velocities, is given by

$$\nu'_{\mathrm{syn}}(\gamma_e) = \frac{3\gamma_e^2 q_e B}{16 m_e c}, \quad (17)$$

where $q_e$ is the electric charge of the electron.

The hydrodynamic evolution becomes adiabatic after

$$T_0 = 0.02(1+z)\left(\frac{\epsilon_B}{0.1}\right)^2\left(\frac{\epsilon_e}{0.1}\right)^2 E_{52} n_1 \text{ days} \quad (18)$$

(Sari et al. 1998). At this stage the typical electron, which radiates around $\nu_{\mathrm{peak}}$, no longer cools on the dynamical time of the system. The cooling frequency $\nu_c$ at a given time is the synchrotron frequency of an electron that cools during the dynamical time. This frequency scales as $\nu_c \propto T^{-1/2}$. On the other hand, the peak frequency scales as $\nu_{\mathrm{peak}} \propto T^{-3/2}$. Since $T_0$ is defined as the time at which $\nu_c = \nu_{\mathrm{peak}}$, we obtain

$$\frac{\nu_c}{\nu_{\mathrm{peak}}} = \frac{T}{T_0}. \quad (19)$$

This means that for $T \gg T_0$ electron cooling does not have a significant effect near the peak frequency, which is the frequency range of interest in this paper.

The adiabatic (BM solution) and the slow cooling approximations are well justified for $T \gg T_0$. Various estimates of the burst parameters yield $E_{52} \sim n_1 \sim 1$ and $\epsilon_e \epsilon_B \sim 0.01$ (Wijers & Galama 1998; Granot, Piran, & Sari 1998; Waxman 1997b). For these values, and for $z \approx 1$, $T_0 \sim 1$ hr. Thus the adiabatic approximation is valid from an hour after the burst and electron cooling can be ignored (around the peak frequency) after about 5 hours. $T_0$ could be large if $\epsilon_e \sim \epsilon_B \sim n_1 \sim 1$. Clearly, our solution is not valid in this case.

We approximate the emission of a single electron as $P_{\nu,e} \propto \nu^{1/3}$ up to the electron typical synchrotron frequency, where we place a cutoff in the emitted power. We normalized the emission function so that the total power emitted by a single electron equals that of an exact synchrotron emission.

Under these assumptions, we obtain, after integration over the power-law electron distribution, that the spectral power per unit volume (in the local frame) at any given point is

$$P'_\nu = \begin{cases} P'_{\nu,\max}\left(\dfrac{\nu}{\nu'_{\min}}\right)^{1/3}, & \nu < \nu'_{\min}, \\ P'_{\nu,\max}\left(\dfrac{\nu}{\nu'_{\min}}\right)^{-(p-1)/2}, & \nu > \nu'_{\min}, \end{cases} \quad (20)$$

where $\nu'_{\min} = \nu'_{\mathrm{syn}}(\gamma_{\min})$ is the synchrotron frequency of an electron with the minimal Lorenz factor at that point. Since the emitted power at each point peaks at $\nu'_{\min}$, this frequency can be looked upon as the typical emitted frequency around which the emitted power is concentrated. Although this emission function was obtained by approximating the spectral emission of each electron as having the shape of the low-frequency tail ($\propto \nu^{1/3}$), the spectral power for the whole electron distribution resembles that obtained for an exact synchrotron emission and an isotropic electron velocity distribution. The solid curve in Figure 4 represents the local emissivity from an exact synchrotron emission of an iso-

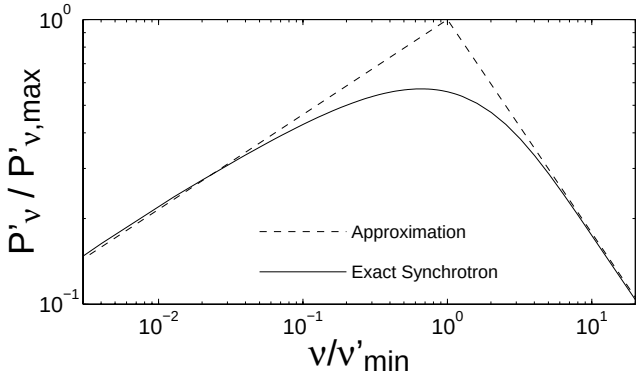


FIG. 4.—Local emissivity from a power-law distribution of electrons, emitting synchrotron radiation. The solid curve represents exact synchrotron emission with an isotropic electron velocity distribution, while the dashed curve represents the approximation we used for the local emissivity. The differences in the local emissivity tend to smear out when integration is performed over the whole volume behind the shock front.

tropic distribution of electrons (Rybicki & Lightman 1979; Wijers & Galama 1998), while the dashed curve represents equation (20) with

$$P'_{\nu,\max} = 0.88\left[\frac{4(p-1)}{3p-1}\right]\frac{n'P'_{e,\mathrm{av}}}{\nu'_{\mathrm{syn}}(\langle\gamma_e\rangle)}\,, \tag{21}$$

where a factor of 0.88 was added to improve the fit to the exact synchrotron emission. In our calculations we use the local emission represented by the dashed line in Figure 4. This local emission differs by up to ~45% from that of an exact synchrotron emission near the peak and is only slightly different above or below the peak. Note that differences in the local emissivity tend to get smeared out when the contribution to the observed flux density is integrated over the whole volume behind the shock front. We expect that considering exact synchrotron emission should somewhat lower the peak flux and the peak frequency, and make the light curve and spectra more rounded and flat near the peak. We evaluate that the peak flux would be lower by about 30%. Since there are only slight differences in high and low frequencies, there should hardly be any effect on the value of the point where the extrapolations of the power laws at high and low frequencies meet (see Table 1).

The results are presented as a function of the dimensionless similarity variable $\phi \equiv \nu/\nu_T$, where $\nu_T$ is defined as the observed synchrotron frequency of an electron with $\gamma_e = \gamma_{\min}$ just behind the shock on the LOS:

$$\nu_T \equiv \nu_{\min}(y=\chi=1)$$
$$= 1.71\times 10^{14}\sqrt{1+z}\,\frac{f(p)}{f(2.5)}\,\epsilon_B^{1/2}\epsilon_e^2 E_{52}^{1/2} T_{\mathrm{days}}^{-3/2}\ \mathrm{Hz}\,, \tag{22}$$

where $f(p) \equiv [(p-2)/(p-1)]^2$. Our results can therefore be looked upon, with the proper scaling of the logarithmic $x$-axis, either as the spectra at a given observed time or as the light curve at a fixed observed frequency.

Similarly, we express the observed flux density in terms of a "standard" flux density $F_0$ defined by

$$F_0 \equiv \frac{N(R_l)P_{\nu,\mathrm{peak}}(1+z)}{4\pi d_L^2}\,,$$
$$P_{\nu,\mathrm{peak}} \equiv 0.88\,\frac{P_{e,\mathrm{av}}(R_l)}{\nu_{\mathrm{syn}}(\gamma_l)} = 0.88\,\frac{P'_{e,\mathrm{av}}(R_l)\gamma_l}{\nu'_{\mathrm{syn}}(\gamma_l)}\,, \tag{23}$$

where $P'_{e,\mathrm{av}}(R_l)$ and $\nu'_{\mathrm{syn}}(\gamma_l)$ are the total power and synchrotron frequency of an average electron at $y=\chi=1$, respectively, $P_{\nu,\mathrm{peak}}$ is an estimate of the peak spectral power of an average electron, and $N(R_l) \equiv 4\pi R_l^3 n_0/3$ is the total number of electrons behind the shock at the time $t$ in the observer frame for which $R(t) = R_l$. Allowing for cosmological corrections, $F_0$ is given by

$$F_0 = 82.4(1+z)\epsilon_B^{1/2} E_{52} n_1^{1/2} d_{L28}^{-2}\ \mathrm{mJy}\,, \tag{24}$$

where $d_{L28}$ is the luminosity distance $d_L$ to the GRB in units of $10^{28}$ cm.

## 4. THE LIGHT CURVES AND SPECTRA

The results for the observed flux density are presented in Figure 5. The flux density arriving from the LOS (*dashed curve*) peaks at $\phi_{\mathrm{peak}} \cong 0.98$, and is only slightly rounded near the peak. The flux density arriving from an infinitely thin shell (*dotted curve*) peaks at $\phi_{\mathrm{peak}} \cong 1.92$ and is quite rounded and flat near the peak. The flux density arriving from the whole volume behind the shock front (*solid curve*) peaks at $\phi_{\mathrm{peak}} \cong 1.88$ and is flat and rounded near the peak, quite resembling the flux density from an infinitely thin shell.

TABLE 1

FEATURES OF THE LIGHT CURVE AND SPECTRA FOR DIFFERENT MAGNETIC FIELD MODELS

| PHYSICAL MODEL | | | | | |
|---|---|---|---|---|---|
| Magnetic Field | $p$ | $\phi_{\mathrm{peak}}$ | $\psi_{\mathrm{peak}}$ | $\phi_{\mathrm{extr}}$ | $\psi_{\mathrm{extr}}$ |
| $B$ | 2 | 2.34 | 0.183 | 4.11 | 0.260 |
| $B$ | 2.5 | 1.88 | 0.205 | 4.66 | 0.313 |
| $B$ | 3 | 1.65 | 0.218 | 5.33 | 0.355 |
| $B_\perp$ | 2.5 | 1.67 | 0.178 | 4.12 | 0.273 |
| $B_{\mathrm{rad}}$ | 2.5 | 2.86 | 0.284 | 7.30 | 0.454 |

NOTE.—$\phi_{\mathrm{peak}}$, $\psi_{\mathrm{peak}}$, $\phi_{\mathrm{extr}}$, and $\psi_{\mathrm{extr}}$ are defined in the text. $\phi_{\mathrm{peak}}$ and $\psi_{\mathrm{peak}}$ are numerical coefficients relating the peak frequency and the peak flux, respectively, to those obtained from simpler analytical models. They are given for different magnetic field models and different values of the electron power law $p$.

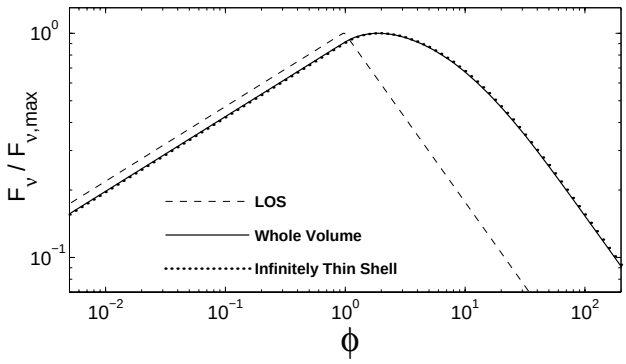


FIG. 5.—Observed flux from synchrotron emission of a power-law electron distribution for the BM solution. The different curves stand for emission only along the LOS, emission from an infinitely thin shell, and emission from the whole volume behind the shock. The emission from the whole volume is very similar to that obtained for an infinitely thin shell, due to a coincidence that arises from our choice for the magnetic field model (see § 5).

Our best prediction for the flux density measured by a distant detector is obtained when we assume a realistic hydrodynamical solution (the BM solution) and a realistic radiation emission and use the general formula (see the solid curve in Fig. 5). We would now like to examine it more closely. The curve looks quite flat near the peak, and we attempt to demonstrate this feature in a quantitative manner. If one compares the peak flux obtained by extrapolation of the power laws, obtained at low and high frequencies, to the "actual" peak flux, one obtains that it is larger by a factor of 1.53: $F_{\rm extr} = 1.53F_{\nu,\rm max}$. In order to further estimate the flatness of the curve near the peak, we define $\phi_+$ and $\phi_-$ by $F_\nu(\phi_+) = F_\nu(\phi_-) = 0.5F_{\nu,\rm max}$, where $\phi_+ > \phi_{\rm peak} > \phi_-$. We obtain that $\phi_- \approx 0.1\phi_{\rm peak}$ and $\phi_+ \approx 10\phi_{\rm peak}$, so that $\phi_+/\phi_- \sim 100$. In a similar manner, we define $T_+$ and $T_-$ for a given observed frequency, by $F_\nu(T_+) = F_\nu(T_-) = 0.5F_{\nu,\rm max}$, where $T_+ > T_{\rm peak} > T_-$. One obtains: $T_+/T_- = (\phi_+/\phi_-)^{2/3} \sim 20$ (note that $T_+/T_-$ is frequency independent).

GRB 970508 displayed a sharp rise in the optical flux just prior to its peak, followed by a power-law decay (Sokolov et al. 1997), showing $T_+/T_- < 3$. This rise is inconsistent with the flat peak of the light curve found here, as can be seen in Figure 6. The power-law decay following the peak was proportional to $T^{-1.18}$ (Sokolov et al. 1997). For slow cooling of the electrons this implies $3(p-1)/4 = 1.18$, i.e., $p = 2.57$, which is the value we used for the fit in Figure 6. To complete the fit, one needs to determine the time and the value of the peak flux. The power-law decay imposes one constraint on these two parameters. We show in Figure 6 three options for the arbitrary choice that is essential in this stage. The values chosen for the peak flux and the time of the peak in the curves depicted in Figure 6 were $R_c = 18.9$; $T_{\rm days} = 0.40$, $R_c = 19.6$; $T_{\rm days} = 0.68$, and $R_c = 20.4$; $T_{\rm days} = 1.19$, respectively, from top to bottom. These values imply constraints on the parameters of the burst, but do not determine them uniquely.

Relaxing the adiabatic assumption, i.e., assuming the hydrodynamic evolution had been radiative at the time of the optical peak, results in an even flatter peak to the light curve (Sari et al. 1998), making it even harder to reconcile it with the observed optical data. Thus, the optical peak of GRB 970508 cannot be associated with the typical frequency crossing the observed band, and other possible explanations for its appearance should be considered. This association is further undermined by the similarity between the features of the optical and X-ray afterglow of GRB 970508 which can be seen in the first day or so (Piro et al. 1998). This similarity might suggest an X-ray peak close in time to the optical peak. Unfortunately, this cannot be tested, because of gaps in the data. It is possible that during the early phase of the afterglow of GRB 970508 there was a continuous emission from the source (Katz, Sari, & Piran 1998). A simultaneous peak in the optical and X-ray afterglow would be quite natural under this interpretation.

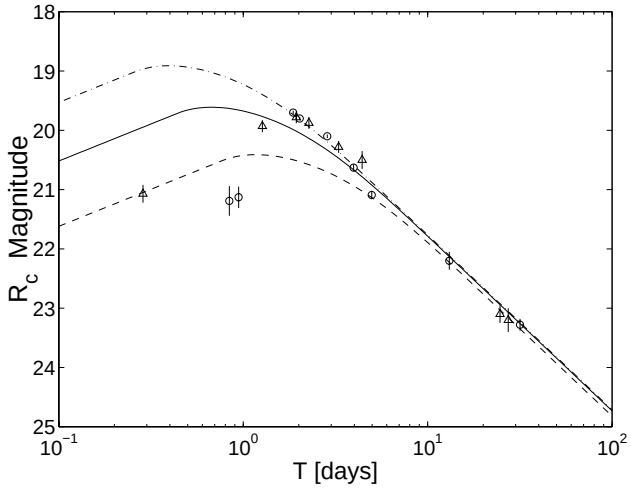


FIG. 6.—Circles and triangles represent optical observations of the afterglow of GRB 970508 (made by Sokolov et al. 1997 and Metzger et al. 1997, respectively). The three curves are possible fits of the light curve we calculated for $p = 2.57$, which fits the power-law decay of the observed flux density from these data. Although the power-law decay fits relatively well, the shape of the observed peak is clearly very different from the flat peak predicted by our calculations.

At a given observed time $T$, the observed flux peaks at

$$\nu_{\rm peak} \equiv \phi_{\rm peak}\,\nu_T = 3.22\times10^{14}\sqrt{1+z} \times \frac{\phi_{\rm peak}(p)}{\phi_{\rm peak}(2.5)}\,\frac{f(p)}{f(2.5)}\,\epsilon_B^{1/2}\epsilon_e^2 E_{52}^{1/2} T_{\rm days}^{-3/2}\ {\rm Hz}\,, \quad (25)$$

where $\phi_{\rm peak}$ is a slowly decreasing function of $p$, and the main dependence on $p$ is through $f(p)$. The maximal flux density is given by

$$F_{\nu,\rm max} \equiv \psi_{\rm peak}\,F_0 = 16.9(1+z)\,\frac{\psi_{\rm peak}(p)}{\psi_{\rm peak}(2.5)}\,\epsilon_B^{1/2} E_{52}\, n_1^{1/2} d_{L28}^{-2}\ {\rm mJy}\,, \quad (26)$$

where $\psi_{\rm peak}$ is a slowly increasing function of $p$.

Two other useful quantities are $\nu_{\rm extr}$, the frequency where the extrapolations of the asymptotic power laws above and below $\nu_{\rm peak}$ meet, and $F_{\rm extr}$, the extrapolated flux density there. The flux density at $\nu_{\rm peak} \ll \nu \ll \nu_c$ (where $\nu_c$ is the cooling frequency) can be approximated by $F_\nu \cong F_{\rm extr}(\nu/\nu_{\rm peak})^{-(p-1)/2}$. For $\nu_a \ll \nu \ll \nu_{\rm peak}$ (where $\nu_a$ is the self-absorption frequency), it can be approximated by $F_\nu \cong F_{\rm extr}(\nu/\nu_{\rm peak})^{1/3}$:

$$\nu_{\rm extr} \equiv \phi_{\rm extr}\,\nu_T = 7.98\times10^{14}\sqrt{1+z} \times \frac{\phi_{\rm extr}(p)}{\phi_{\rm extr}(2.5)}\,\frac{f(p)}{f(2.5)}\,\epsilon_B^{1/2}\epsilon_e^2 E_{52}^{1/2} T_{\rm days}^{-3/2}\ {\rm Hz}\,, \quad (27)$$

$$F_{\rm extr} \equiv \psi_{\rm extr}\,F_0 = 25.8(1+z)\,\frac{\psi_{\rm extr}(p)}{\psi_{\rm extr}(2.5)}\,\epsilon_B^{1/2} E_{52}\, n_1^{1/2} d_{L28}^{-2}\ {\rm mJy}\,, \quad (28)$$

where $\phi_{\rm extr}$ and $\psi_{\rm extr}$ are both slowly increasing functions of $p$. The values $\phi_{\rm peak}$, $\psi_{\rm peak}$, $\phi_{\rm extr}$, $\psi_{\rm extr}$ for representative values of $p$ are given in Table 1.

These results can be best understood by looking at the "egg" that constitutes the locus of points from which photons reach the detector simultaneously, and mapping upon it the typical emitted frequency in the observer frame. Figure 7 depicts the lines of equal $\nu_{\rm min} = \nu_{\rm syn}(\gamma_{\rm min})$. From the electron distribution we obtain that $\langle\gamma_e\rangle = \gamma_{\rm min}/[f(p)]^{1/2}$ and therefore: $\nu_{\rm min} = f(P)\nu_{\rm syn}(\langle\gamma_e\rangle)$. For this reason, the frequency contour lines that are depicted in Figure 7 also represent lines of equal typical synchrotron frequency $\nu_{\rm syn}(\langle\gamma_e\rangle)$.

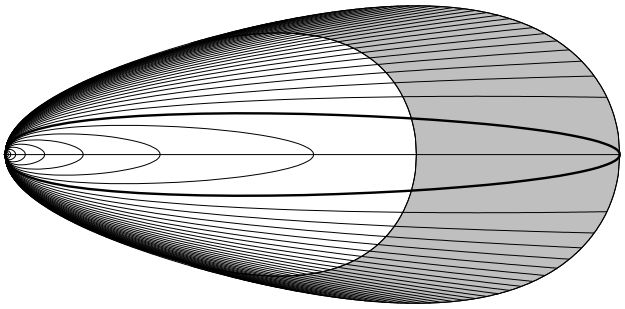

FIG. 7.—Equal observed synchrotron frequency contour lines, at a given observed time, for the BM solution. Each line represents a different value of $\phi$. The bold contour line is $\phi = 1$. The lines are separated by a constant logarithmic interval in $\phi$: $\Delta \log_{10} \phi = 0.05$ (inner contour lines, which cross the LOS, represent $\phi < 1$). The shaded region represents a finite shell of thickness $\Delta = R/4\gamma^2$ in the observer frame.

There are two opposing factors that determine the shape of the observed synchrotron frequency contour lines that are depicted in Figure 7. The shift from the local frame to the observer frame, $\nu' = \nu\gamma(1 - \beta\nu)$, causes the frequency to decrease as one moves away from the LOS. However, at earlier emission times, and at locations closer to the shock front, the typical synchrotron frequencies in the local frame are higher, and so is the Lorentz factor of the matter. This tends to increase the observed frequencies of photons that were emitted earlier (i.e., from the back of the egg) and closer to the shock (i.e., closer to the surface of the egg).

The result of these two opposing effects, for the BM solution is that, as one goes backward along the LOS to earlier emission times, the observed synchrotron frequency for a constant observed time is almost independent of $\chi$: $\nu_{\rm syn}(\mathrm{LOS}) \propto \chi^{-1/24}$. This explains the result for the flux density arriving from the LOS (Fig. 5, *dashed curve*), namely, that the peak flux is obtained at a frequency just slightly lower than $\nu_T$: $\phi_{\rm peak} \cong 0.98$, and the light curve is only slightly rounded near the peak. The fact that $\nu_{\rm min} < \nu_T$ along the LOS accounts for the fact that the peak flux is obtained at $\phi_{\rm peak} < 1$. The fact that the decrease in $\nu_{\rm min}$ as one goes back along the LOS is very moderate means that in order for the emitted radiation to be concentrated around a frequency substantially lower than $\nu_T$, one has to go very deep in the radial profile along the LOS to $r \ll R_l$. This implies that one gets far from the shock front (to $\chi \gg 1$), and therefore the contribution obtained to the total flux density is small. For this reason $\phi_{\rm peak}$ is very close to 1.

The observed flux density from an infinitely thin shell peaks at $\phi_{\rm peak} \cong 1.92$, and the light curve (or spectrum) is quite rounded and flat near the peak (see Fig. 5, *dotted line*). This result can be understood by following the surface of the "egg" (see Fig. 7); $\nu_{\rm min}$ increases as one goes to the back of the egg (i.e., to earlier emission times) along its surface, and it does so much faster than it decreases when one goes back along the LOS. Therefore, one gets a substantial contribution to the flux density at $\phi > 1$, before one gets too far back in the shell, where the total contribution to the flux density drops considerably. This explains why the peak flux for an infinitely thin shell is obtained at a frequency significantly higher than $\nu_T$, whereas for the LOS it is obtained at a frequency only slightly lower than $\nu_T$.

In order to demonstrate the importance of accounting for synchrotron emission from the full fireball, we consider a simpler model of a monochromatic emission from a uniform shell. The emission frequency at every point is set to be the synchrotron frequency of an electron with the average Lorentz factor at that point: $\nu_{\rm syn}(\langle\gamma_e\rangle)$, where $\langle\gamma_e\rangle$ and $\nu_{\rm syn}$ are taken from equations (16) and (17), respectively. The emitted power per unit volume per unit frequency in the local frame is given by

$$P'_{\nu'} = n' P'_{e,\rm av}\, \delta(\nu' - \nu'_{\rm syn}) \,, \tag{29}$$

where $P'_{e,\rm av}$ is given by equation (16).

We calculate the observed flux density due to this emission within a thin shell of matter, of finite thickness $\Delta$ in the observer frame. This case was calculated numerically by Waxman (1997c). He took $\Delta = \zeta R/\gamma^2$, which corresponds in our notation to $\chi_{\rm max}(\zeta) = 1 + 16\zeta$. We use equation (13), and integrate only up to $\chi_{\rm max}(\zeta)$. Substituting $g(\chi) = 1$ in equation (13), we obtained an analytic solution which is shown in Figure 8. The results are expressed by the similarity variable $\phi \equiv \nu/\nu_T$, where in this case $\nu_T$ is obtained by dropping $f(p)$ from equation (22).

Figure 8 depicts the observed flux density for a few values of $\zeta$, including $\zeta \to 0$. It is very different from Figure 5. This difference can be intuitively understood by looking at Figure 9, which depicts the frequency contour lines for a uniform shell. In contrast to Figure 7, the frequency contour lines are nearly perpendicular to the LOS and higher frequencies come from the back of the "egg" (i.e., from smaller radii). For this reason the flux density vanishes for $\phi < 1$ (see Fig. 8). For every value of $\zeta$ there exists a critical frequency $\phi_c(\zeta)$ for which the frequency contour line touches the back of the shell, exactly on the LOS. This is demonstrated by the bold frequency contour line in Figure 9, which represents $\phi_c$ for $\zeta = \frac{1}{4}$, and touches the back of the shell exactly on the LOS at point C. The flux density peaks exactly at $\phi_c(\zeta)$. From our analytical solution for a uniform thin shell we obtained a simple analytical expression for the time (or frequency) of the peak flux as a function of $\zeta$:

$$\phi_{\rm peak}(\zeta) = \phi_c(\zeta) = (1 + 16\zeta)^{3/2} \,. \tag{30}$$

The resulting spectra and light curve for a uniform shell are qualitatively different from those obtained when full hydrodynamical radial profile and synchrotron emission are considered. For a uniform shell, the rather arbitrary choice of $\zeta$ determines the time of the peak flux for a given

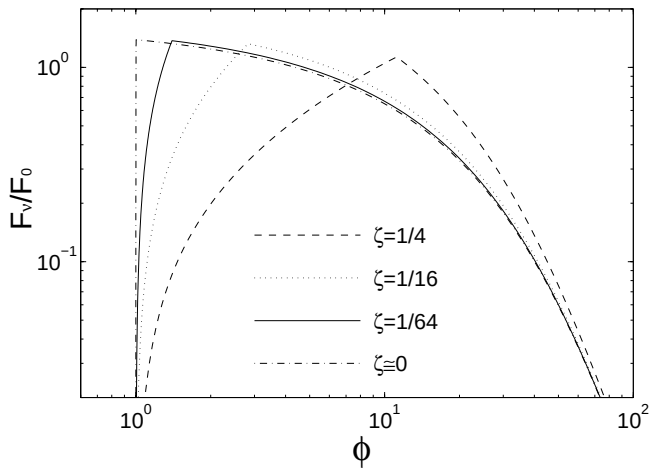


FIG. 8.—Observed flux density from a uniform shell, for different values of the shell thickness in the observer frame: $\Delta \equiv \zeta R/\gamma^2$. The value of $\phi$ at the peak is a function of the shell thickness (see eq. [30]).

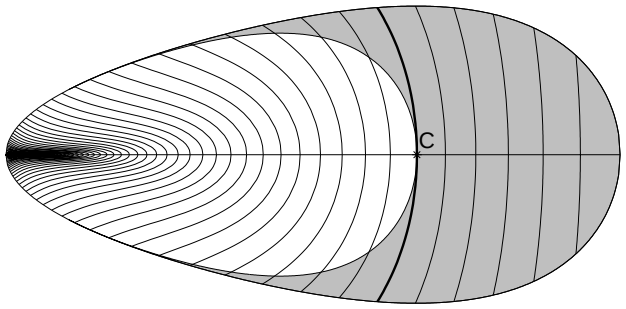


FIG. 9.—Equal observed synchrotron frequency contour lines, at a given observed time, for a uniform shell. The lines (*right to left*) represent $\phi = 5^{1/4}, 5^{2/4}, 5^{3/4}, \ldots$. The typical synchrotron frequency is larger than $\nu_T$ everywhere (everywhere $\phi > 1$), and $\phi$ increases as one goes to the back (i.e., to the left) of the "egg" along the LOS, to smaller radii. The shaded region represents a finite shell of thickness $\Delta = R/4\gamma^2$ in the observer frame. The bold frequency contour line that touches the back of the shell on the LOS at point C represents the frequency for which the flux density from a uniform shell, considered in this section, peaks.

observed frequency, and the peak is substantially sharper, with a smaller width at half-maximum. This illustrates the need of using a realistic hydrodynamic solution and a realistic emission.

## 5. ALTERNATIVE MAGNETIC FIELD MODELS

Although the hydrodynamic profile is given by the BM solution, the structure and profile of the magnetic field are less clear. So far we have assumed that everywhere the magnetic field energy is a fixed fraction of the internal energy:

$$e'_B \equiv \frac{B^2}{8\pi} = \epsilon_B e' \ . \tag{31}$$

Since not much is known about the origin or spatial dependence of the magnetic field, we consider now two alternative models for the magnetic field. There is no compelling reason to prefer one of these models over the others. The consideration of alternative models serves just to explore the effect that a variation of the magnetic field has on our results. Although quantitative differences exist between the models, they are small. This also serves, in a way, as a test for the generality of our results.

We assume that each matter element acquires a magnetic field according to equation (31) when it passes the shock. The two alternative models are obtained by assuming that the magnetic field is either radial or tangential, and evolves according to the "frozen field" approximation.

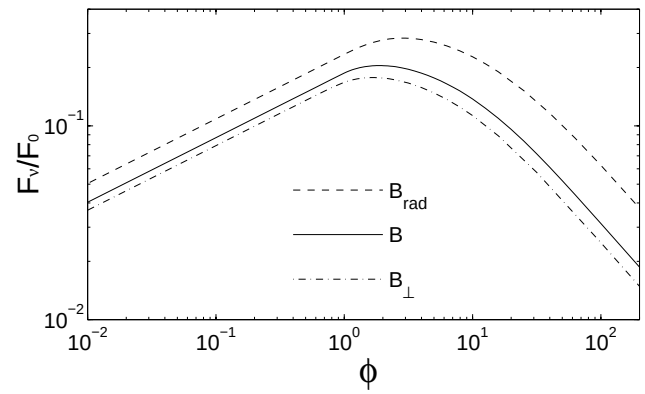


FIG. 10.—Observed flux density for three different magnetic field models. $B_{\rm rad} = B = B_\perp$ on the shock front, while behind the shock front $B_{\rm rad} > B > B_\perp$.

Consider a small matter element, which passes the shock at a time $t_0$ in the observer frame. Just after it passes the shock it possesses a magnetic field $B_0$ (in the local frame) given by equation (31). We consider a cubic volume $V_0 = L^3$ (in the local frame) with one face perpendicular to the radial direction. According to the BM solution, at a later time $t$ this matter element will be at $\chi = [R(t)/R(t_0)]^4$, and it will occupy a box of a size $L_{\rm rad} = \chi^{9/8}L$ in the radial direction, and a size $L_\perp = \chi^{1/4}L$ in the two tangential directions ($\hat{\phi}$ and $\hat{\theta}$). One also obtains that $B_0 = B_f \chi^{3/8}$, where $B_f$ is the magnetic field at the front of the radial profile, just behind the shock, at the time $t$. We consider two possibilities for the direction of the magnetic field at $t_0$: a radial and a tangential magnetic field, $B_{\rm rad}$ and $B_\perp$. Our previous "equipartition" model will be denoted simply by $B$. In both new cases the "frozen field" approximation implies that the magnetic field will remain in the same direction, while its magnitude changes in the following way:

$$B_{\rm rad} = B_f \chi^{-1/8} \ , \quad B = B_f \chi^{-17/24} \ , \quad B_\perp = B_f \chi^{-1} \ . \tag{32}$$

Using the general formula (eq. [13]), we obtain now the observed flux density for $B_{\rm rad}$ and $B_\perp$ (see Fig. 10). Some of the features are summarized in Table 1. Since the emission from the shock front ($\chi = 1$) is identical in all three cases, the results obtained for an infinitely thin shell in the previous section, including the dotted curve in Figure 5, are still valid here. This implies that the difference between the various curves in Figure 10 arises from the radial integration. Our previous model for the magnetic field led to an almost negligible effect of the radial profile (see Fig. 5). Now we find that, generally, the effect of the radial integration is comparable to that of the angular integration, as the flux density for $B_{\rm rad}$ and $B_\perp$ are substantially different than for an infinitely thin shell.

From equation (32) we can see that $B_{\rm rad}$ implies a larger magnetic field than $B$, and therefore a larger total emission and higher emission frequencies, while $B_\perp$ implies a smaller magnetic field than $B$, and therefore a smaller total emission and lower emission frequencies. This is consistent with the results in Table 1, namely, $\phi_{\rm peak}(B_{\rm rad}) > \phi_{\rm peak}(B) > \phi_{\rm peak}(B_\perp)$ and $\psi_{\rm extr}(B_{\rm rad}) > \psi_{\rm extr}(B) > \psi_{\rm extr}(B_\perp)$. An important feature that appears in all the magnetic field models we considered is the flatness of the peak: $\phi_+/\phi_- \sim 100$–$120$ and $T_+/T_- \sim 21$–$24$.

## 6. THE OBSERVED IMAGE

We turn now to calculate the observed image, as seen by a distant observer. We consider the BM hydrodynamic solution. Substituting $g(\chi) = \chi^{-1}$ in equation (13), we obtain

$$dF_\nu = \frac{8R_l^3(1+z)}{d_L^2} \frac{P' y^{10} \chi}{(1+7\chi y^4)^2} \, dy \, d\chi \ . \tag{33}$$

We calculate the surface brightness (energy per unit time per unit frequency per unit area perpendicular to the LOS) at a given arrival time $T$. The distance of a point from the LOS is given by

$$R_\perp \equiv r \sin\theta \cong R_l y \sqrt{1-\mu^2} \cong \frac{\sqrt{2}R_l}{4\gamma_l} \sqrt{y - \chi y^5} \ . \tag{34}$$

The maximal value of $R_\perp$ is obtained on the surface of the "egg" (where $\chi = 1$), implying $y = 5^{-1/4}$. The observed

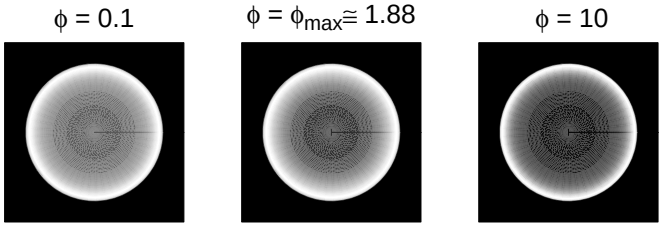


FIG. 11.—Observed image of a GRB afterglow, for different values of $\phi$. The different images can represent either the image at different frequencies at the same observed time or the image at the same frequency at different observed times. In the latter case, one should also remember that the size of the observed image increases with the observed time as $R_{\perp,\max} \propto T^{5/8}$. A larger value of $\phi$ represents a higher observed frequency or a later observed time. The image is brighter near the edge and dimmer near the center, and the contrast is higher at large values of $\phi$.

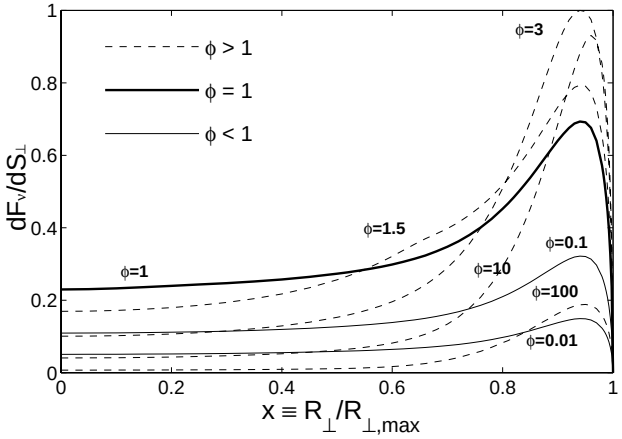


FIG. 12.—Observed surface brightness as a function of $x \equiv R_\perp/R_{\perp,\max}$, for different values of $\phi$. The surface brightness peaks near the outer edge of the image, drops sharply towards the edge ($x = 1$), and decreases more gradually toward the center. The normalization preserves the correct ratio between the absolute surface brightness, for the different values of $\phi$, which decreases both for low and for high values of $\phi$.

image at a given observed time $T$ is restricted to a disk of radius $R_{\perp,\max} \cong 4.14\gamma_l cT$ around the LOS. Using equation (12), we obtain an explicit expression for the BM solution:

$$R_{\perp,\max} = 3.91 \times 10^{16} \left(\frac{E_{52}}{n_1}\right)^{1/8} \left(\frac{T_{\rm days}}{1+z}\right)^{5/8} \text{cm} . \quad (35)$$

We calculate the surface brightness within this disk, and find it useful to work with the variable: $x \equiv R_\perp/R_{\perp,\max}$. The differential of the area on this disk is given by

$$dS_\perp = 2\pi R_\perp \, dR_\perp \equiv 2\pi R_{\perp,\max}^2 \, x \, dx . \quad (36)$$

Using equation (34), we obtain from equation (33)

$$\frac{dF_\nu}{dS_\perp} = \frac{4}{\pi} \left(\frac{R_l}{d_L}\right)^2 \frac{(1+z)^2}{cT} \frac{P' y^5 \chi}{(1+7\chi y^4)^2} \, dy , \quad (37)$$

from which we obtain, after integration, the surface brightness as a function of $R_\perp$. In this expression, $\chi$ should be taken as a function of $y$ for a given $x$, according to equation (34). The limits of the integration over $y$ are determined from the condition $\chi > 1$.

We calculated the surface brightness for several values of $\phi$, and, as before, the different images can be viewed either as the observed images at a given observed time at different observed frequencies or as the observed images at a given frequency at different observed times. The observed images are quite similar for the different magnetic field models we considered, and therefore we present detailed results only for $B$ (Figs. 11 and 12), and summarize in Table 2 the features of the images obtained for $B_{\rm rad}$, $B$, and $B_\perp$.

The observed image is bright near the edge and dimmer at the center. At high values of $\phi$ (high frequencies or late observed times) the surface brightness at the center is only a few percent of the maximal surface brightness, which is obtained near the edge ($x \sim 0.93$–$0.95$), and a bright ring is clearly seen with a sharp edge on the outer side and a more gradual decrease in the surface brightness toward the center. At $\phi < 1$ (low frequencies or early observed times) the surface brightness at the center is around 0.32–0.39 of the maximal surface brightness, and, though the image is brighter near the edge, the center should be visible as well (see the left image in Fig. 11).

The observed image calculated considering emission only from the surface of the shock front (Sari 1998) yielded a surface brightness diverging at $R_{\perp,\max}$. This divergence is an artifact of the assumption that the radiation is emitted from a two-dimensional surface. Other features of the image, such as the difference between high and low frequencies, are quite similar to those found here.

The transition in the distribution of the relative surface brightness along the observed image, between the limiting cases of small and large $\phi$, occurs over 1 order of magnitude in $\phi$: $1 < \phi < 10$. The relative surface brightness hardly changes beyond this region (although the absolute surface

TABLE 2

FEATURES OF THE OBSERVED IMAGE

| | SB($x = 0$)/SB$_{\max}$ | | $\phi < 1$ | | $\phi \gg 1$ | |
|---|---|---|---|---|---|---|
| MAGNETIC FIELD MODEL | $\phi < 1$ | $\phi \gg 1$ | $x_{\rm peak}$ | $\Delta x$ | $x_{\rm peak}$ | $\Delta x$ |
| $B_\perp$ | 0.32 | 0.034 | 0.95 | 0.263 | 0.96 | 0.151 |
| $B$ | 0.34 | 0.039 | 0.94 | 0.296 | 0.95 | 0.178 |
| $B_{\rm rad}$ | 0.39 | 0.065 | 0.93 | 0.403 | 0.90 | 0.290 |

NOTE.—We define $\Delta x \equiv x_+ - x_-$, where $x_+ > x_-$ are the values of $x \equiv R_\perp/R_{\perp,\max}$ at which the surface brightness (SB) drops to half of its maximal value. $\Delta x$ is an estimate for the width of the bright ring that appears on the outer edge of the image; $x_{\rm peak}$ is the value of $x$ for which the maximal SB is obtained, and its values indicate that the SB peaks near the outer edge of the image. It is evident that the contrast between the center and the edge of the image is considerably larger for high frequencies (or late times) than for low frequencies (or early times).

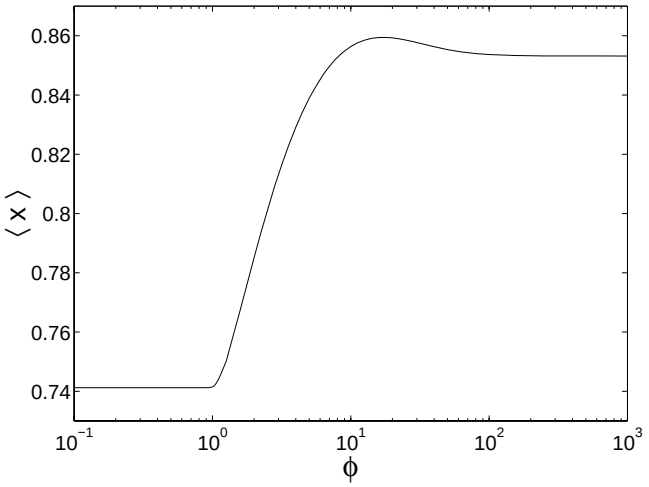


FIG. 13.—Flux-averaged value of $x \equiv R_\perp/R_{\perp,\max}$ as a function of $\phi$; $\langle x \rangle \approx 0.74$ for $\phi < 1$, and $\langle x \rangle \approx 0.85$ for $\phi \gg 1$.

brightness drops both for low and for high values of $\phi$, due to the drop in the observed flux density).

The fact that at a given observed time the relative surface brightness at the center of the image is smaller for high frequencies than it is for low frequencies may be intuitively understood: for high frequencies the emittance decays in time, and is therefore lower at large radii, which correspond to small values of $x \propto R_\perp$, which are located at the center of the image.

To calculate the effects of scintillation or microlensing, one needs a good estimate of the effective size of the observed image. We therefore calculate the flux-averaged value of $x$:

$$\langle x \rangle = \frac{\int x\, dF_\nu}{\int dF_\nu} . \tag{38}$$

A plot of $\langle x \rangle$ as a function of $\phi$ is shown in Figure 13. For $\phi < 1$ one obtains that $\langle x \rangle$ is constant: $\langle x \rangle \cong 0.74$. As $\phi$ increases above unity, $\langle x \rangle$ increases, until it reaches its maximal value of $\langle x \rangle \cong 0.86$ at $\phi \approx 17$. Above this value of $\phi$ there is a slight decrease in $\langle x \rangle$ as $\phi$ increases, until for $\phi \gg 1$ it reaches the limiting value: $\langle x \rangle \cong 0.85$. These values are slightly lower than those obtained for an infinitely thin shell: $\langle x \rangle \cong 0.79$ for $\phi \ll 1$ and $\langle x \rangle \cong 0.91$ for $\phi \gg 1$. (Note that Panaitescu & Mészáros 1998 and Sari 1998, who also considered the infinitely thin shell approximation, obtained slightly different erroneous results.)

## 7. DISCUSSION

We have calculated the observed flux density from a spherical adiabatic relativistic blast wave described by the self-similar Blandford & McKee (1976) solution. We have considered synchrotron emission from a power-law distribution of electrons, using a realistic local emissivity, which depends on the local hydrodynamic parameters.

We have calculated the peak frequency and the peak flux (eqs. [25] and [26]) as a function of the observed time. The value we obtained for the peak frequency is a factor of $\sim 1.8$ smaller than the value obtained by Sari et al. (1998), a factor of $\sim 2.5$ (for $p = 2.5$) smaller than the value obtained by Wijers & Galama (1998), and a factor of $\sim 35$ (for $p = 2.5$) smaller than the value obtained by Waxman (1997b). This large difference from the last result is partly due to the fact that Waxman (1997b) assumes that the peak frequency is the synchrotron frequency of an average electron $\nu_{\rm syn}(\langle \gamma_e \rangle)$, while the peak frequency is actually much closer to $\nu_{\rm syn}(\gamma_{\rm min})$—the synchrotron frequency of an electron with the minimal Lorentz factor. The value we obtained for the peak flux is a factor of $\sim 1.9$ (for $p = 2.5$) smaller than the value obtained by Wijers & Galama (1998), a factor of $\sim 5.1$ larger than the value obtained by Waxman (1997b), and a factor of $\sim 6.5$ smaller than the value obtained by Sari et al. (1998).

We have also calculated the frequency and the flux density at the point where the asymptotic high- and low-frequency power laws intersect (eqs. [27] and [28]). Like the expressions for the peak frequency and the peak flux (eqs. [25] and [26]), these expressions are given in terms of numerical corrections $\phi_{\rm peak}$, $\phi_{\rm extr}$, $\psi_{\rm peak}$, $\psi_{\rm extr}$ to the results of a simpler analytic model. Thus, using these values (given in Table 1 and below the equations mentioned above), one can modify the results of such an analytic calculation. This might be particularly important when one is trying to fit the observed light curve or spectrum to a theoretical model.

Both the light curve and the spectra are flat near the peak. The flux density at a given observed time drops to half its maximal value at around 1 order of magnitude from the peak frequency, on either side. The flux density at a given observed frequency drops to half its maximal value at a factor of $\sim 5$ before and after the time of the peak flux. This result was obtained for all the magnetic field models we considered, and it therefore seems to be of quite a general nature. We have used an approximate form for the local synchrotron emissivity. We expect that without this approximation the values of the peak flux and the peak frequency would be slightly lower, and the light curve and the spectrum would be even more rounded and flat near the peak.

In contrast to the flatness of the peak, discussed above, GRB 970508 displayed a sharp rise in the optical flux density, immediately followed by a power-law decay (Sokolov et al. 1997). Sari et al. (1998) considered both radiative and adiabatic evolution of the blast wave, and found that the steepest rise in the flux density occurs before the peak, for an adiabatic evolution and slow cooling of the electrons, which is the case discussed in this paper. This steepest rise is $T^{1/2}$, and, as we have shown in this paper, the rise in the flux decreases as the peak is approached, and the peak itself is quite flat. We obtained $T_+/T_- \sim 21$–$24$, which indicates a flat peak, while GRB 970508 displayed $T_+/T_- < 3$. This rules out the interpretation of the optical peak of GRB 970508 as the peak of the light curve, predicted by the existing fireball models. It therefore appears that another explanation is needed. The peak in the light curve might be a result of continuous emission from the source (Katz, Sari, & Piran 1998).

In order to demonstrate the importance of accounting for synchrotron emission from the full fireball, we also considered monochromatic emission from a uniform shell (Waxman 1997c), for which the results change drastically. In particular the location of the peak flux depends critically on the width of the shell $\zeta$ (see eq. [30]), which is chosen quite arbitrarily.

The image of a GRB afterglow looks like a ring, even when emission is considered from the whole volume behind the shock front. Similar results were obtained for simpler

models (Waxman 1997c; Sari 1998; Panaitescu & Mészáros 1998). The image is bright near the edge and dimmer at the center. The contrast in the surface brightness between the center and the edge of the image increases and the ring is narrower at higher frequencies (optical and X-ray). For low frequencies (as long as self-absorption is not significant) the contrast is smaller and the ring is wider. The best available resolution is obtained in radio frequencies, which can be considered as "low frequencies" for the first few months. Thus, the afterglow of a future nearby GRB ($z \sim 0.2$) might be resolved in radio. This model predicts that in early times, when $\nu_{\rm radio} < \nu_{\rm peak}$, the image should appear as a relatively wide ring with a relatively small contrast, while for later times, where $\nu_{\rm radio} > \nu_{\rm peak}$ (as long as the relativistic regime is not exceeded), the image should appear as a narrow ring and possess a large contrast.

This research was supported by NASA grant NAG5-3516, and US-Israel grant 95-328. R. S. thanks the Clore Foundation for support.

REFERENCES

Blandford, R. D., & McKee, C. F. 1976, Phys. Fluids, 19, 1130 (BM)
Granot, J., Piran, T., & Sari, R. 1998, ApJ, submitted (astro-ph/9808007)
Katz, J. I. 1994, ApJ, 422, 248
Katz, J., & Piran, T. 1997, ApJ, 490, 772
Katz, J., Sari, R., & Piran, T. 1998, Phys. Rev. Lett., 80, 1590
Mészáros, P., & Rees, M. 1997, ApJ, 476, 232
Metzger, M. R., et al. 1997, IAU Circ. 6676
Panaitescu, A., & Mészáros, P. 1998, ApJ, 493, L31
Paczyński, B., & Rhoads, J. 1993, ApJ, 418, L5
Piran, T. 1994, in AIP Conf. Proc. 307, Second Huntsville Workshop on Gamma-Ray Bursts, ed. G. J. Fishman, J. J. Brainerd, & K. Hurley (New York: AIP), 495
Piro, L., et al. 1998, A&A, 331, L41
Rybicki, G. B., & Lightman, A. P. 1979, Radiative Processes in Astrophysics (New York: Wiley Interscience)
Rees, M. 1966, Nature, 211, 468
Sari, R. 1997, ApJ, 489, L37
———. 1998, ApJ, 494, L49
Sari, R., & Piran, T., 1997, ApJ, 485, 270
Sari, R., Piran, T., & Narayan, R. 1998, ApJ, 497, L17
Sokolov, V. V., et al. 1998, A&A, in press (astro-ph/9709093)
Waxman, E. 1997a, ApJ, 485, L5
———. 1997b, ApJ, 489, L33
———. 1997c, ApJ, 491, L19
Wijers, R. A. M. J., & Galama, T. J. 1998, ApJ, submitted (astro-ph/9805341)